

# Entropy Density Benchmarking of Near-Term Quantum Circuits

Marine Demarty,<sup>1,\*</sup> James Mills,<sup>1</sup> Kenza Hammam,<sup>1</sup> and Raúl García-Patrón<sup>1,2</sup>

<sup>1</sup>*School of Informatics, University of Edinburgh,  
10 Crichton Street, Edinburgh EH8 9AB, U.K.*

<sup>2</sup>*Phasecraft Ltd.,  
77-79 Charlotte Street, London W1T 4PW, U.K.*

Understanding the limitations imposed by noise on current and next-generation quantum devices is a crucial step towards demonstrations of quantum advantage with practical applications. In this work, we investigate the accumulation of entropy density as a benchmark to monitor the performance of quantum processing units. A combination of analytical methods, numerical simulations, and experiments on programmable superconducting quantum circuits is used to build a simple yet practical heuristic model of entropy accumulation based on global depolarising noise. This demonstrates the potential of such an approach to construct effective heuristic models. The monitoring of entropy density not only offers a novel and complementary approach to existing circuit-level benchmarking techniques, but more importantly, it provides a much needed bridge between circuit-level and application-level benchmarking protocols. In particular, our heuristic model of entropy accumulation allows us to improve over existing techniques to bound the circuit size threshold beyond which quantum advantage is unattainable.

Keywords: Benchmarking, Entropy, Purity, Variational Quantum Algorithms, Quantum Advantage

## I. INTRODUCTION

One of the main limitations of current and near-term quantum devices remains the imperfect control of the qubits and the challenge of isolating the system from its environment, leading to noise levels beyond those required to reach fault-tolerant quantum computation [1–3]. The current regime is known as noisy intermediate-scale quantum (NISQ) computation. Even if noise greatly limits the computational power of such computers, their practical applications are worth investigating as their size is already above the limit of 50 qubits - which is typically when error-free quantum devices become hard to simulate by a classical digital computer [4, 5].

To harness the full power of NISQ technology, however, one must look for tasks that are suitable for intermediate-scale devices with high error rates: this means, for instance, designing quantum algorithms that are resilient to noise, and finding tests of quantum advantage that do not require more than a few hundreds of qubits. Example of such tasks include random circuit sampling [6] and gaussian boson sampling [7, 8] which have been the target of recent quantum supremacy claims. However, these sampling tasks have very limited useful applications (see e.g., [9–11]).

A popular way to design applications for NISQ devices is to reformulate a given computational task

as an optimisation problem which can be solved using so-called variational quantum algorithms (VQA) [12]. These hybrid quantum-classical algorithms are believed to be good candidates to implement on NISQ devices affected by errors and low coherence times. Solving combinatorial optimisation problems [13] or finding the ground-state energy of a Hamiltonian [14] are examples among an extensive literature on the topic [12]. Whether quantum advantage can be achieved in the near term on *practical* tasks remains a question of scientific debate, as seen after the recent simulation of the behaviour of a magnetic material on a 127-qubit quantum processor [15] and its subsequent rebuttals, e.g., [16, 17].

To understand and evaluate the potential of noisy quantum devices to solve specific tasks, it is crucial to be able to assess the effect of errors on performance. With this in mind, a wide range of benchmarking techniques have been developed. Those fall into three main categories: gate, circuit, and application-level protocols. Gate-level benchmarking protocols aim at characterising the performance of low-level components such as gates and sequences of gates (e.g., randomized benchmarking [18], gate-set tomography [19]). Circuit-level protocols are concerned with assessing the performance of a quantum processing unit (QPU) when running specific classes of circuits (e.g., cross-entropy benchmarking [6], quantum volume [20]). Lastly, application-level benchmarking techniques characterise the performance of a QPU when solving practical problems (e.g., Q-score for MAX-CUT with Quan-

---

\* marine.demarty@ed.ac.uk

tum Approximate Optimization Algorithm (QAOA) [21], fermionic depth for many-body problems [22]). However, to the best of our knowledge, those benchmarking categories are relatively isolated and there are no benchmarks that exploit benchmarking tools of one level to provide information at a higher level.

A significant part of the errors affecting quantum circuits, such as stochastic Pauli channels, lead to an increase of entropy. Intuitively, the accumulation of entropy is bad for the performance of the system, as the entropy quantifies closeness to a maximally mixed quantum state. The link between entropy accumulation and the performance of variational quantum algorithms was recently formalised in [23], providing a rigorous formalism that bridges the gap between circuit and application-level benchmarking. Other work on the entropy has mainly focused on characterising entanglement evolution within a circuit by looking at the entropy of a partition of the system or entanglement entropy as opposed to the entropy of the whole system (see e.g., [24–27]).

In this work, we investigate the use of entropy density accumulation as a novel and complementary circuit-level metric to monitor the performance of near-term quantum devices. We demonstrate that a combination of analytical methods, numerical simulations and experiments allows to build simple yet effective heuristic models of entropy accumulation. More importantly, we show how entropy density benchmarking bridges circuit-level and application-level benchmarking protocols, enabling us to derive more accurate thresholds than in [23] on the circuit size above which quantum advantage is unattainable.

The structure of this paper is as follows. In section II, we analyse the Renyi-2 entropy scaling of the output register of a hardware-efficient VQA circuit with the circuit size (width and depth) and noise parameters numerically. This allows us to build an analytical model for entropy accumulation in such circuits based on global depolarising noise which we compare with experimental data on a superconducting device in section III. We then show how our model may be used to decide whether quantum advantage is attainable with a specific device for a specific optimisation problem in section IV. Lastly, we summarise the main results of this paper and give possible future directions to this work in section V.

## II. CLASSICAL SIMULATION

We are interested in how the entropy of the quantum register evolves in a variational quantum circuit

as layers of gates are applied to the input state causing errors to accumulate, and in the dependency of the entropy on the circuit width (number of qubits). As a worked example, we consider a typical hardware-efficient VQA ansatz: each layer of this circuit consists of the concatenation of random single-qubit rotations about the  $X$  axis  $R_X(\theta) := \exp(-i\frac{\theta}{2}X)$  with random single-qubit rotations about the  $Y$  axis  $R_Y(\theta) := \exp(-i\frac{\theta}{2}Y)$ , followed by a set of nearest neighbours  $CZ$  gates distributed into two layers of non-intersecting gates, as shown in Fig. 1.

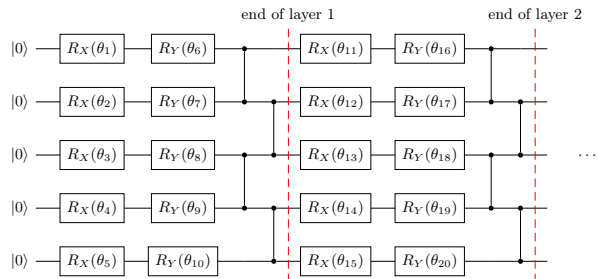


Figure 1: First two circuit layers of a 5-qubit hardware-efficient parameterised quantum circuit  $U(\vec{\theta})$ . Each circuit layer is composed of a single-qubit  $R_X(\theta)$  rotation followed by a  $R_Y(\theta)$  rotation and a final layer of  $CZ$  gates between nearest neighbours. The angles  $\theta_i$ s are drawn from the uniform distribution over  $[0, 2\pi)$ .

### A. Entropy density accumulation under local depolarising noise

We start by numerically investigating the entropy accumulation of our circuit of interest for different circuit widths, number of circuit layers (depth), under a commonly used local depolarising noise model. Let  $p_1$  (resp.  $p_2$ ) be the depolarising probability for single-qubit (resp. two-qubit gates). The noise model we choose for the numerical simulation consists of applying a single-qubit (resp. two-qubit) depolarising channel with depolarising probability  $p_1$  (resp.  $p_2$ ) after each single-qubit (resp. two-qubit) gate of the quantum circuit from Fig. 1. For a single-qubit state  $\rho$ , our single-qubit depolarising channel is  $\mathcal{N}_{p_1}(\rho) := (1 - p_1)\rho + p_1I/2$  while for a two-qubit state  $\rho$ , the two-qubit depolarising channel considered is  $\mathcal{N}_{p_2}(\rho) := (1 - p_2)\rho + p_2I/4$ .

We use the software development kit Qiskit [28] to calculate the entropy of the quantum register

at depth  $D$  by evolving the density matrix of  $n$  qubits starting with the input state  $\rho_0 := (|0\rangle\langle 0|)^{\otimes n}$ . For each circuit layer we compute the second-order Renyi entropy defined as

$$S^{(2)}(\rho_D) = -\log_2(\text{Tr}[\rho_D^2]), \quad (1)$$

where  $\rho_D$  is the output density matrix (after applying  $D$  layers of gates). The obtained evolution of the Renyi entropy density  $S^{(2)}(\rho_D)/n$  for different numbers of qubits  $n$  (widths) and different depths can be found in Fig. 2, where for  $p_1$  and  $p_2$  we took deduced values from QPU calibration data (see appendix E). We focus our interest on entropy density in order to allow a meaningful comparison between circuits of different width with the additional benefit of potentially inferring universal rules independently of the system size. Remark that for every circuit size and depth, the dotted results correspond to the classical simulation using local depolarising noise, while the solid lines correspond to an interpolation given by a global depolarising model discussed in the subsection below.

As expected, local depolarising noise causes the system to converge towards the maximally mixed state as the error occurrence increases, approaching a density of 1 at high depth. Interestingly, the larger the width  $n$  of the circuit, the faster the entropy density converges, where for large systems  $n \rightarrow \infty$  the speed of convergence of the Renyi entropy density seems to saturate to an asymptotic bound detailed below.

## B. Global depolarising heuristic model

### 1. Analytical model

We wish to build a heuristic model for the evolution of the second-order Renyi entropy as a function of the quantum circuit size i.e. depth and width. To achieve that, we explore the approximation of the chosen local depolarising noise model described previously by a global depolarising noise channel applied after the last layer of the ideal quantum circuit  $U_D(\vec{\theta})$ , i.e. the output of our noisy VQA circuit can be written as

$$\rho_D = (1 - P)U_D(\vec{\theta})\rho_0U_D(\vec{\theta})^\dagger + P\frac{\mathbf{I}}{2^n}, \quad (2)$$

where  $P$  is the global depolarising probability, and  $\rho_0 = (|0\rangle\langle 0|)^{\otimes n}$  is the input state. The analytical model for the purity then reads

$$\text{Tr}[\rho_D^2] = (1 - 2^{-n})((1 - P)^2 - 1) + 1. \quad (3)$$

To link the global depolarising probability  $P$  of the model with the circuit size  $(n, D)$  and local noise parameters  $(p_1, p_2)$ , we exploit the standard assumption that the probability of no error occurring in the circuit under local depolarising noise should match the probability of no error occurring in the model with global depolarising noise. This yields

$$1 - P = (1 - p_1)^{|\text{1Q gates}|}(1 - p_2)^{|\text{2Q gates}|}, \quad (4)$$

$$= e^{-\alpha_1 2nD} e^{-\alpha_2(n-1)D}, \quad (5)$$

where  $|\text{1Q gates}|$  (resp.  $|\text{2Q gates}|$ ) is the number of one-qubit (resp. two-qubit) gates of the circuit, corresponding to  $2n$  and  $n - 1$  respectively for the circuit of Figure 10.

We have introduced the parameters  $\alpha_1 := \ln((1 - p_1)^{-1})$ ,  $\alpha_2 := \ln((1 - p_2)^{-1})$  which are expected to model the depolarising probabilities  $(p_1, p_2)$  in the low noise limit:  $\alpha_1 \approx p_1$  and  $\alpha_2 \approx p_2$ . Substituting Eq. (3) with Eq. (5), we get the following model for the purity:

$$\text{Tr}[\rho_D^2] = (1 - 2^{-n})(e^{-2(2\alpha_1 n + \alpha_2(n-1))D} - 1) + 1, \quad (6)$$

with fitting parameters  $\alpha_1, \alpha_2$ .

We subsequently performed a non-linear least squares fitting of the purity data obtained from numerical simulation; the corresponding Renyi-2 entropy density data (dots) with the Renyi-2 entropy density of the fitted purity model are shown in Fig. 2. We explored three different strategies for the use of the free parameters  $\alpha_i$ : (i) leaving both parameters free  $\alpha_i$ ; (ii) fixing  $\alpha_1 = 0$ ; (iii) assuming  $\frac{\alpha_1}{\alpha_2} = \frac{p_1}{p_2}$ ; where the last two assumption are different approaches to model the gap between single-qubit and two-qubit gate errors. If all the three assumptions lead to very similar qualities of interpolation, the first one leads to parameters  $\alpha_1$  and  $\alpha_2$  that have little connection with the physical values  $p_1$  and  $p_2$ . Therefore, we used the constraint  $\frac{\alpha_1}{\alpha_2} = \frac{p_1}{p_2}$  in all the fittings presented in this manuscript, to guarantee the same order of magnitude between all pairs  $(\alpha_i, p_i)$ .

Interestingly, a global depolarising model provides a good heuristic description of the entropy accumulation behaviour without having to average over the whole family of circuits (variational gate parameters), it achieves a good fit already for a given specific circuit.

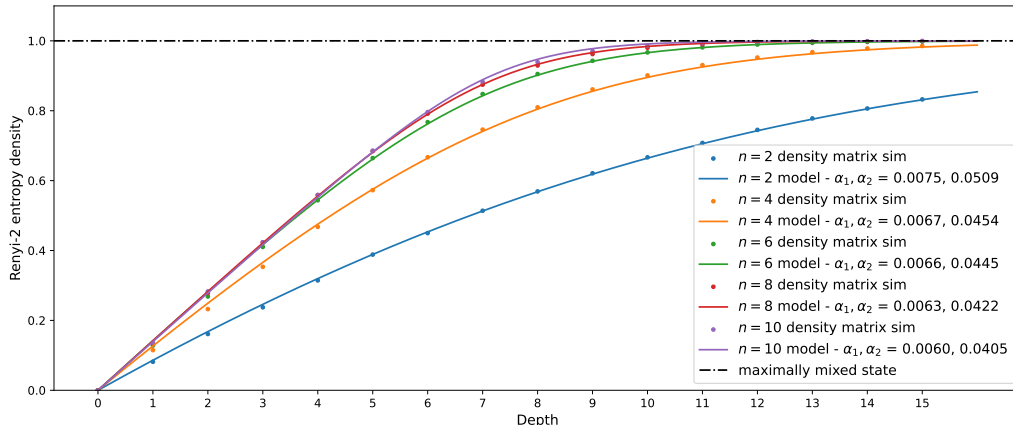


Figure 2: **Numerical simulation and heuristic model.** We simulate a single VQA circuit represented in Fig. 1, with randomly selected parameters (random seed `np.random.seed(837)`) affected by local depolarising noise ( $p_1 = 0.008$  and  $p_2 = 0.054$  from calibration data of Rigetti’s QPU, Aspen-M-3). The dots characterize the Renyi-2 entropy density evolution of the quantum register after each circuit layer for different number of qubits  $n$  (see color label). The black horizontal dash-dotted line corresponds to the entropy density of the maximally mixed state  $\sigma_0 := I/2^n$ . The solid lines correspond to interpolations using a global depolarising heuristic model from Eq. (6) with fitting parameters  $\alpha_1$  and  $\alpha_2$  ( $\alpha_i \approx p_i$ ), as detailed in subsection II B 1.

## 2. Asymptotic behaviours

It is easy to see that for the limit  $D \rightarrow \infty$ , the global depolarising model leads to  $\text{Tr}[\rho_D^2] \sim 1/2^n$ , which results in  $S^{(2)}(\rho_D)/n \sim 1$ , reaching the entropy density of the maximally mixed state as observed in Fig. 2.

For all system sizes, at small enough circuit depth, one can observe in Fig. 2 that the Renyi entropy density growth is well approximated by a linear function with the circuit depth. In the limit of large system sizes  $n \rightarrow \infty$ , the Renyi entropy density growth converges to an upper bound whose analytical expression reads

$$\lim_{n \rightarrow +\infty} \frac{S^{(2)}(\rho_D)}{n} = \begin{cases} \frac{2(2\alpha_1 + \alpha_2)}{\ln(2)} D & \text{if } D \leq \frac{\ln(2)}{2(2\alpha_1 + \alpha_2)} \\ 1 & \text{if } D > \frac{\ln(2)}{2(2\alpha_1 + \alpha_2)} \end{cases}, \quad (7)$$

which defines the depth threshold

$$D^* = \frac{\ln(2)}{2(2\alpha_1 + \alpha_2)} \quad (8)$$

above which the output is indistinguishable from the maximally mixed state. For instance, taking typical QPU values for noise parameters  $\alpha_1 = p_1 = 3 * 10^{-4}$  and  $\alpha_2 = p_2 = 1 * 10^{-3}$  [29], we get a depth thresh-

old  $D^* = 217$  beyond which the quantum device’s output is no better than a random guess.

## III. EXPERIMENTAL STUDY AND ENTROPY ESTIMATION METHODS

We are now ready to study entropy accumulation as a function of circuit size on an actual quantum processing unit, and explore whether our model for the Renyi-2 entropy or equivalently purity from Eq. (6) matches experimental results. We focus on two techniques: the classical shadows protocol and a SWAP test-based approach. In subsection III A 3, we provide detailed analytical, numerical, and experimental data over a superconducting platform using classical shadows, a technique that has proven extremely useful for the estimation of expectation values on NISQ devices. Unfortunately, the sampling cost for entropy estimation using classical shadows scales exponentially with the system size, which motivates the comparison with the SWAP test, which should be efficient in sample count but requires a more complex quantum circuit. Unexpected technical limitations due to the topology and gate error of the device made our SWAP data inconclusive.

We therefore complement the experimental study of classical shadows with a detailed numerical comparison of the SWAP test and classical shadows assuming local depolarising noise in subsection III B 2. We also analysed the accumulation of entropy on a trapped-ion quantum computer using the SWAP test method as a proof of concept, however, we do not provide the results here as they cannot be easily compared with those obtained on a superconducting QPU.

## A. Classical Shadows

### 1. Background

In their 2020 paper, Huang *et al.* introduce a new method for efficient estimation of many properties of a quantum state  $\rho$  known as the classical shadows protocol [30]. Instead of performing full tomography of the quantum state which requires a number of measurements that scales exponentially with the system size  $n$ , they proposed to obtain several classical snapshots of the quantum state by measuring the state in  $M$  randomly chosen basis  $K$  times. Classical post-processing of the measurement outcomes then allows to deduce the expectation value of  $N_{obs}$  observables of interest  $\text{Tr}[O_i\rho]$ , in a sample efficient manner for local observables.

Huang *et al.* propose two versions of this protocol: (i) random single-qubit Pauli measurements; (ii) random  $n$ -qubit Clifford circuit measurements. Pauli measurements are particularly efficient for predicting a large collection of local observables, and

only require short depth measurement circuits which are very suitable for NISQ devices. On the other hand,  $n$ -qubit Clifford measurements should be preferred for efficiently predicting many global observables with a bounded Hilbert-Schmidt norm; the main drawback is that of order  $n^2/\log(n)$  gates are needed for their implementation, resulting in circuits that are less practical for current quantum devices.

More precisely, to estimate  $N_{obs}$  observables  $O_i$  with additive error  $\epsilon$ , the number  $M$  of randomly chosen bases measured  $K$  times, needs to scale as

$$O(\log(N_{obs}) \max_i \|O_i\|_{shadow}^2/\epsilon^2), \quad (9)$$

where  $\|O_i\|_{shadow}$  is the so-called shadow norm, which is upper bounded by  $\max_i 4^{k_i} \|O_i\|_\infty^2$  in scenario (i) of single-qubit Clifford measurements and  $\max_i \text{Tr}[O_i^2]$  in scenario (ii) of global Clifford measurements (see [30]), where  $k_i$  is the locality of observable  $O_i$  and  $\|\cdot\|_\infty$  is the operator norm.

### 2. Renyi-2 entropy estimation

The above framework also extends to non-linear functions of  $\rho$ , such as quadratic terms  $\text{Tr}[O_i\rho \otimes \rho]$ . By noting that the second-order Renyi entropy of a quantum state,  $S^{(2)}(\rho)$ , is a function of the purity  $\text{Tr}[\rho^2]$  which can be rewritten as

$$\text{Tr}[\rho^2] = \text{Tr}[S\rho \otimes \rho], \quad (10)$$

where  $S$  is the SWAP matrix, one can use the classical shadows protocol to build an estimate for the second-order Renyi entropy where the corresponding purity is estimated as

$$\hat{P}_{\text{Shadows}} = \frac{2}{M(M-1)} \sum_m \sum_{m'|m'<m} \frac{1}{K^2} \sum_{k,k'=1}^K \prod_{n=1}^N \left(9 \times \gamma_{n,m,m',k,k'} - 4\right), \quad (11)$$

where  $n$  labels the qubits,  $k, k'$  the snapshot of a given measurement  $m$ , and  $\gamma_{n,m,m',k,k'} \in \{0, 1/2, 1\}$  depends on the measurement and its outcome as given in appendix B in the case of Pauli measurements. Because the operator  $S$  is not local, the use of classical shadows to estimate purities requires an exponential scaling of the number of samples with system size.

Although the Renyi-2 entropy or equivalently purity is a global property, here, we chose to consider

Pauli basis measurements for entropy estimation on *near-term* devices. This is because a single layer of single-qubit gates is easy to implement and introduces fewer errors compared to an  $n$ -qubit Clifford circuit. Fig. 3 shows the corresponding measurement circuit. For large quantum systems, the Pauli version of the method is very inefficient in terms of sampling cost, as the purity is a global property thus implying a  $4^n$  scaling with the system size  $n$ : fixing  $\epsilon, \delta > 0$ , obtaining an  $\epsilon$ -accurate pu-

rity estimate with success probability  $1 - \delta$  requires  $O(\ln(\frac{1}{\delta}) \times \frac{4^n}{\epsilon^2})$  (Pauli) measurements (see appendix B). Note that the  $n$ -qubit Clifford version of the protocol would only provide a quadratic improvement of the scaling, as the number of measurements scales as  $\text{Tr}[O_i^2] = \text{Tr}[S^2] = 2^n$ . We expect that the added complexity of the circuit will make this approach unpractical with current devices.

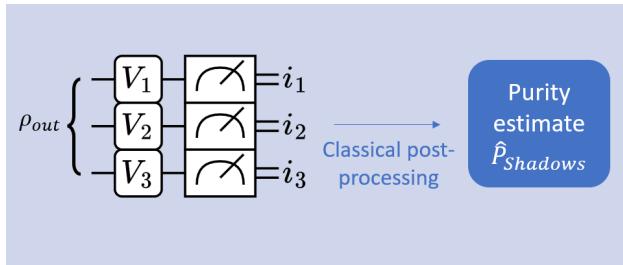


Figure 3: **Classical shadows protocol.** Each  $V_i$  is a single-qubit Clifford gate such that its combination with a computational basis measurement corresponds to a random measurement in the  $X$ ,  $Y$ , or  $Z$  basis.

### 3. Experimental study of entropy accumulation

Using the Pauli version of the classical shadows protocol with purity estimate given in Eq. (11), we estimate the purity and the Renyi-2 entropy density of the output state of the chosen VQA circuit as functions of circuit depth on Rigetti’s Aspen-M-3 QPU (see appendix E). Experimental results for a width  $n = 3$  circuit can be found in Fig. 4, using two different estimation strategies (see discussion in subsection III A 5 below for details) shown with light and dark golden error bars, where for each instance, a purity estimate was calculated by taking  $K = 1,000$  classical snapshots of the output state for each of the  $M = 50$  measurement settings consider.

We compare the hardware purity and entropy experimental results with numerical simulations of the same VQA circuits followed by its classical post-processing under the same sample constraints as for the hardware experiments, where we assumed a local depolarising noise model (see light blue error bars in Fig. 4) with parameters  $p_1 = 0.008$  and  $p_2 = 0.054$  deduced from calibration data of Aspen-M-3 (see appendix E). We also consider a variant of the last simulation that includes measurement errors from calibration data (see appendix E) which corresponds to the dark blue error bars. Finally, we also ex-

tract the purity and Renyi-2 entropy from a density matrix emulation (solid black lines). Remark that the difference between the light blue error bars and black line, is that the last one is the exact expectation value of the former whenever the classical shadows average converges to the right expectation value. This is generally the case for sufficiently large number of measurements and sufficiently large number of qubits experiments, but can lead to some subtle behaviour for experiments with small numbers of qubits as detailed below in subsection III A 5.

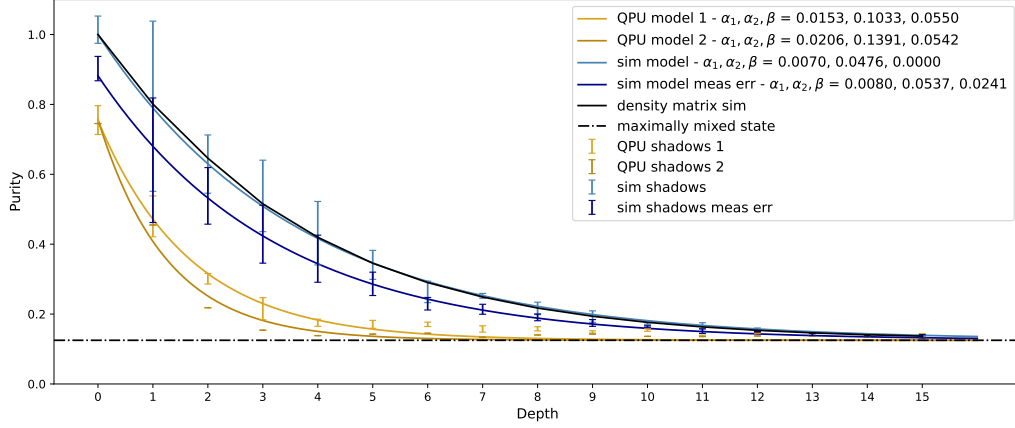
Similarly as before, we performed a non-linear least squares fitting on the purity of both the experimental data (light and dark golden) and numerical simulation of the classical shadow protocol results (light and dark blue). To account for the additional measurement circuit (cf. Fig. 3) and potential readout errors which increase the entropy, we introduce an additional fitting parameter  $\beta$  in our heuristic model from Eq. (6) (see appendix A). The results are shown in Fig. 4.

### 4. Discussion of results

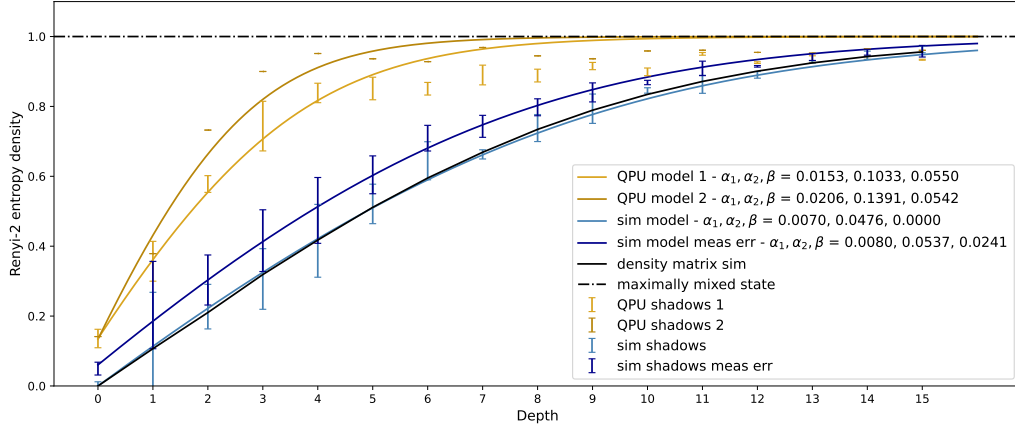
One can notice in Fig. 4 that the heuristic global depolarising noise model, despite capturing most of the entropy accumulation behaviour, also slightly differs from experimental data (golden error bars) at large depth where the Renyi entropy density converges to a value close to but not quite the upper-bound given by maximally-mixed states and reaches its asymptotic value with mild oscillatory dynamics. This has been confirmed by further experiments run for circuits with up to depth 30. We believe that both the presence of entropy-decreasing types of noise, such as amplitude damping, and coherent errors could explain this phenomenon.

As for the adapted global depolarising heuristic model (dark blue line) described in appendix A, we observe that its fitted parameters  $\alpha_1, \alpha_2, \beta$  successfully match calibration data  $p_1 = 0.008, p_2 = 0.054, p_m \approx P(0|1) = 0.03$  used in the local depolarising noise simulations with readout errors (dark blue error bars).

We also observe that experimentally (golden error bars) the entropy grows faster than predicted by classical simulation based on calibration data from the device (light blue error bars). Even after accounting for readout errors to our numerical simulations (see dark blue error bars), a gap remains between the experimental hardware entropy accumulation and the one predicted by a local depolarising noise model. Although an unexpected systematic



(a) Purity



(b) Renyi entropy density

Figure 4: **Experimental results and validation of our heuristic model.** We consider a VQA circuit as in Fig. 1 applied to  $n = 3$  qubits, with fixed circuit parameters (fixed random seed `np.random.seed(837)`). Golden error bars give the purity and Renyi-2 entropy evolution as functions of circuit depth on Rigetti's QPU Aspen-M-3 using two different methods. Each error bar was obtained by running the classical shadows protocol 3 times, and computing the average estimate and the standard deviation over those 3 samples. Results obtained in the same setting but using a local depolarising noise model ( $p_1 = 0.008$  and  $p_2 = 0.054$  from calibration data of Aspen-M-3) correspond to the blue error bars; dark (resp. light) blue error bars were obtained with (resp. without) readout errors from calibration data ( $P(0|1) = 0.03$  and  $P(1|0) = 0.02$ ). The black solid lines show the purity and Renyi-2 entropy density evolution obtained via density matrix simulation under our local depolarising noise model without measurement errors (similar to light blue error bars). The black horizontal dash-dotted lines correspond to the purity or entropy density of the maximally mixed state  $\sigma_0 := I/2^n$ . Fit of our global depolarising heuristic model, where we have imposed that  $\alpha_2/\alpha_1 = p_2/p_1$ , and where  $\beta$  models readout errors and noise in the measurement circuit, corresponds to the solid golden and blue lines.

error may not be fully discarded, the most likely explanation for this observed difference may be the interaction of depolarising noise with other sources of error, like damping, coherent errors and cross-talks.

### 5. Randomisation of measurements

A standard classical shadows protocol should ideally randomly select a new measurement for every measurement sample. Changing circuits being relatively costly in execution time for some platforms like superconducting qubits, we often implement a variant where  $M$  measurement settings are randomly selected and each one is executed  $K$  times its number of occurrence. Because our experiments were limited in number of qubits ( $n = 3$ ) and therefore we were expecting to see the occurrence of most measurements and in similar number, we initially opted to derandomise the measurement choice and scan the  $3^3 = 27$  possible measurement settings with  $K = 1,000$  classical snapshots of the output state for each of them. We were surprised to observe that this strategy generated a systematic error on the experimental entropy estimation that were later corroborated by numerical simulations (see appendix B 3). To mitigate this bias, we reintroduced a random choice of measurements in our experimental results (light and dark golden error bars in Fig. 4) through two different methods of simulating random measurement choices from our experimental data retrieved from a deterministic choice of measurements.

We proceeded as follows. We first select  $M = 50$  random measurements and count how many times each measurement is chosen. In method 1 (light golden error bars), we build the list of shadows for a given run of the protocol by replicating the available snapshots of the corresponding set the number of times that the measurement setting has been chosen. Since we still have three sets of data, we can still obtain errors bars.

In method 2 (dark golden crosses), we build the purity estimate for a single run of the protocol by exploiting the three available sets of snapshots for each measurement setting. More precisely, for a given setting, the first three times a measurement occurs, we use one of the three sets of data, and if a measurement occurs more times, we cycle over them again.

## B. SWAP Test

It is easy to realise from the relation in Eq. (10) that the purity of a quantum state can be obtained from a Hadamard test based on a controlled-SWAP operator that has as input two copies of  $\rho$ , as shown in Fig. 5a, a protocol also called SWAP test [31]. While the original protocol was designed to measure the overlap of two pure states, it is well-known that applying the protocol to two copies of the same noisy quantum state gives a measure of its purity from the bias of the Hadamard test outcomes, i.e.,  $\text{Tr}[\rho_{out}^2] = P(0) - P(1) = \langle (-1)^i \rangle$ .

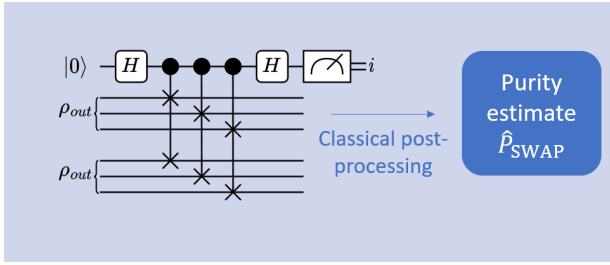
### 1. NISQ-friendly SWAP test

The controlled unitary in the Hadamard test makes its implementation on NISQ devices complex. Fortunately, if one is solely interested in the measurement outcomes, the Hadamard test can be replaced by a measurement in the eigenbasis of the unitary, which for the SWAP test corresponds to a set of Bell state measurements followed by additional post-processing, corresponding to the parity of the collection of the logical AND operations of each Bell measurement [32]. The simplified circuit is depicted in Fig. 5b.

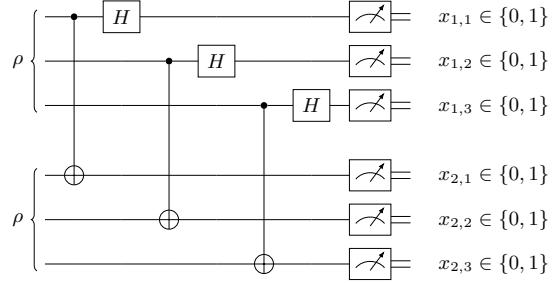
Despite requiring two copies of  $\rho_{out}$ , we see from Fig. 5b that this entropy estimation technique will be very suitable for NISQ devices with a square or similar lattice topology or for platforms with all-to-all connectivity like some ion-traps and neutral-atoms. In the case of superconducting circuits with planar architectures, lattice configurations allow for the Bell measurements to be performed in parallel between neighbouring qubits, thus requiring only one layer of gates for entropy estimation. For other topologies, however, in the worst case, the depth of the measurement circuit will scale linearly with the system size  $n$ .

Hoeffding's inequality gives that at most  $O(\ln(\frac{1}{\delta}) \times \frac{1}{\epsilon^2})$  measurements will be necessary to obtain an  $\epsilon$ -accurate purity estimate with success probability  $1 - \delta$  (see appendix C). That is, an exponential improvement over the classical shadows protocol. However, this comes with the additional cost of running two circuits in parallel, which can lead to additional experimental difficulties.





(a) SWAP test-based protocol.



(b) Simplified SWAP test protocol.

**Figure 5: SWAP test protocol for purity and Renyi-2 entropy estimation.** In Fig. 5a, the SWAP test circuit from [31] is applied to two copies of the quantum state of interest  $\rho_{out}$ . The measurement statistics of the upper qubit can be linked to the purity via  $Tr[\rho_{out}^2] = P(i=0) - P(i=1)$ . In Fig. 5b, Bell state measurements between two copies of the quantum state of interest  $\rho$  allow to estimate its purity via some additional post-processing on the measurement statistics [32]: the measurement outcome  $i$  of the standard SWAP test protocol from Fig.5a is the parity bit of the bitwise AND of  $x_1 := x_{1,1}x_{1,2}\dots x_{1,n} \in \{0,1\}^n$  and  $x_2 := x_{2,1}x_{2,2}\dots x_{2,n}$ , i.e.,  $i = \text{parity}(x_1 \& x_2)$  (see appendix C).

## 2. Comparison of entropy estimation methods

We compare the two entropy estimation methods introduced previously via numerical simulation. Purity and Renyi-2 entropy as functions of circuit depth are shown in Fig. 6 for a width  $n = 5$  VQA circuit for the two techniques of interest: classical shadows (in blue) and the SWAP test (in salmon). The results were obtained using the Aer classical simulator from Qiskit and a local depolarising noise model (with  $p_1 = 0.008$  and  $p_2 = 0.054$  from QPU calibration data).

For both protocols, the same sample complexity of 24,300 measurements was used, where the classical shadows protocol uses  $M = 243$  randomly selected measurement settings and  $K = 100$  shots. As before, for each data point (error bar) the entropy estimation protocol was run 3 times to obtain error bars. Purity and Renyi-2 entropy computed directly from the density matrix under a model of local depolarising noise correspond to the black solid lines.

We observe in Fig. 6 that for measuring the purity the SWAP test protocol performs better on purer states than on mixed states, as shown by the increase in the length of the error bars as we increase the circuit depth and the state becomes more mixed. Intuitively, the more mixed the state is the more unbiased the two outcomes of the Hadamard test become, and therefore more samples are needed to get an  $\epsilon$ -accurate purity estimate. Interestingly, the opposite happens for the classical shadows protocol: its purity estimation is more accurate (smaller stan-

dard deviation for several runs of the protocol) for mixed states in general than for pure states.

Lastly, we observe in Fig. 6 a slight systematic deviation between exact purity or entropy (black line) and estimated values via SWAP test approach (salmon error bars). We believe this could be explained by gate errors in the Bell measurement circuit, composed of  $n$  parallel two-qubit (CNOT) and single-qubit gates (Hadamard). Note that it is possible that such systematic error also exists for the classical shadows protocol due to the single layer of noisy Pauli gates preceding the computational basis measurement, however, single-qubit gate errors are typically an order of magnitude lower and the systematic deviation remains unobserved for the system sizes we have investigated. Remark that the systematic errors discussed above are of a different kind than the ones resulting from derandomising classical shadows measurement choices for small circuit widths discussed in III A 5.

## IV. QUANTUM ADVANTAGE BENCHMARKING

In this section, we show how to combine the design of heuristic models of entropy accumulation in VQA circuits, such as the global depolarising noise model from Eq. (6), with the application-level quantum advantage benchmarking technique introduced in [23]. This allows to make quick reliable predictions on whether the accumulation of errors precludes from reaching quantum advantage or the lat-

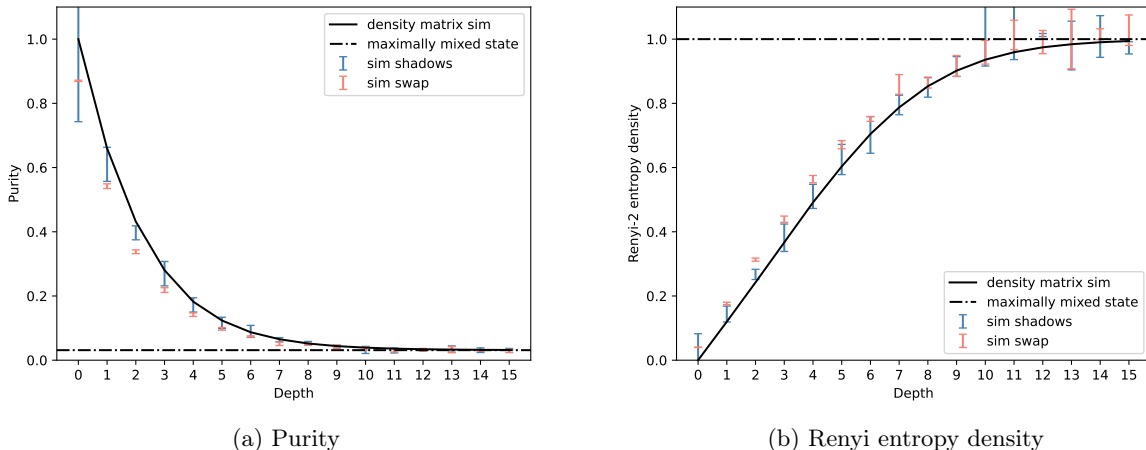


Figure 6: **Entropy estimation methods comparison via numerical simulation.** We consider a VQA circuit as in Fig. 1 applied to  $n = 5$  qubits, with fixed circuit parameters (fixed random seed `np.random.seed(837)`), under local depolarising noise ( $p_1 = 0.008$  and  $p_2 = 0.054$  from calibration data of Rigetti’s Aspen-M-3). Error bars give the purity and Renyi-2 entropy evolution as functions of circuit depth using two entropy estimation protocols and Qiskit’s Aer classical simulator: in blue for the classical shadows technique and in salmon for the SWAP test approach. For both methods, estimates were obtained by performing 24,300 measurements of the VQA circuit, and running the entropy estimation protocol 3 times to get error bars. The black solid lines show the exact purity and Renyi-2 entropy density evolution obtained via density matrix simulation. The black horizontal dash-dotted lines correspond to the purity or entropy density of the maximally mixed state  $\sigma_0 := I/2^5$ .

ter remains possible. Most importantly, one does not need to run the quantum processing unit to solve the targeted application; only a model of how entropy accumulates on the problem-specific circuit ansatz is required. In what follows, we revisit the analysis of [23] for MAX-CUT, but the technique is widely translatable to other optimisation problems, whether defined by classical (e.g., combinatorial optimisation problems [33]) or quantum Hamiltonians (e.g., quantum chemistry problems [34, 35]).

### A. Background

As detailed in [23], given a quantum device and known state-of-the-art classical solver solution to MAX-CUT, we can certify whether there is some potential for a QPU to outperform the best classical solvers or conversely that quantum advantage is out of reach.

This is ascertained by an approach summarised in Fig. 7. Combining a lower bound on the quantum device energy density solution  $\text{Tr}[H\rho_{out}]/n$  as a function of the von Neumann entropy  $S(\rho_{out})/n$

(blue solid line) with the classical solver energy density prediction (red horizontal line) defines an entropy density threshold  $S(\rho_{out})/n \geq c$  (red dotted vertical line) beyond which the QPU cannot provide a better solution than the classical solver.

Despite the benchmarking approach of [23] being constructed for von Neuman entropies and our gathered experimental data being for the Renyi-2 entropy, the well-known bound between the von Neumann and the Renyi entropies  $S(\rho) \geq S^{(2)}(\rho), \forall \rho$ , implies that any conclusion obtained replacing  $S(\rho)$  by  $S^{(2)}(\rho)$  in the analysis summarised in Fig. 7 is a conservative and valid prediction.

### B. Bounds on quantum advantage via circuit-size bounds

The next step of the approach is to combine the previous entropic threshold with the selected heuristic model of entropy accumulation in order to find a bound on the number of gates or maximum circuit depth before our QPU of interest can be certified to not provide better solutions than a standard classi-

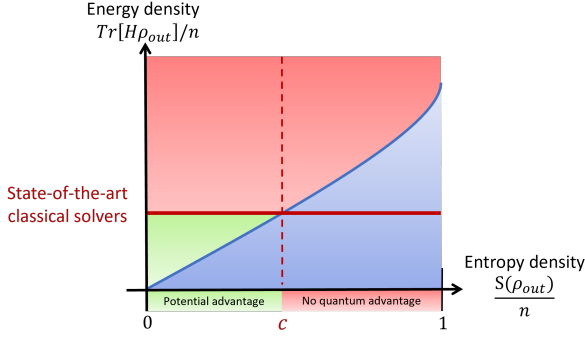


Figure 7: **Quantum advantage benchmarking framework from [23]**. For an optimisation task of the form  $\min_{\rho} \text{Tr}[H\rho]$ , the authors derive a lower bound (blue solid line) on the quantum device’s solution to the energy density ( $\text{Tr}[H\rho_{out}]/n$ ) as a function of the accumulated entropy density ( $S(\rho_{out})/n$ ). The state-of-the-art classical solvers’ solution to this optimisation problem (red horizontal line) defines an entropy density threshold  $c$  such that if the quantum device’s candidate solution  $\rho_{out}$  satisfies  $\frac{S(\rho_{out})}{n} \geq c$  then quantum advantage is out of reach for this device and for this optimisation problem.

cal solver. In what follows we revisit the analysis for MAX-CUT in [23] but now equipped with heuristic models of entropy accumulation.

### 1. Circuit-bounds

Now using a global depolarising heuristic model for the second-order Renyi entropy of the output of the VQA ansatz described in Eq. (6), we obtain the following bound on the circuit size (width  $n$  and depth  $D$ ):

$$2(2\alpha_1 n + \alpha_2(n-1))D \geq \ln \left( \frac{2^n - 1}{2^{n(1-c)} - 1} \right). \quad (12)$$

Assuming that 2-qubit gate depolarising noise is the dominant source of noise on the device ( $\alpha_2 = p_2 \neq 0$ ), which is generally the case in practice, and thus neglecting single-qubit gate depolarising noise ( $\alpha_1 = 0$ ), this yields

$$(n-1)D \geq \frac{1}{2p_2} \ln \left( \frac{2^n - 1}{2^{n(1-c)} - 1} \right), \quad (13)$$

where we assume that  $p_2$  is below 1%, a reasonable assumption for current QPUs. For large problem

size  $n \rightarrow \infty$ , this leads to the bound on the circuit depth (number of circuit layers):

$$D \geq \frac{1}{2p_2} c \ln(2). \quad (14)$$

Note the similarity with the depth threshold obtained in Eq. (8) for large systems  $n \rightarrow \infty$ . In the special case where two-qubit gate depolarising noise dominates ( $\alpha_1 = 0, \alpha_2 = p_2$ ), both depth thresholds differ by the scalar factor  $c$  resulting from the entropy density threshold analysis above.

### 2. Comparison with previous work

Gset is a set of instances of MAX-CUT popular for performance benchmarking for which classical solvers solutions and times to solution are known. Following [23], we use the G12 instance of Gset consisting of 800 nodes and 1,600 edges. Using equation Eq. (13) and the plot of the bound for this MAX-CUT instance from [23] where the entropy density threshold against a heuristic classical solver reads  $c = 0.3$ , we conclude that for  $D \geq 0.104/p_2$ , quantum advantage is out of reach for a quantum device with two-qubit gate depolarising probability  $p_2$ ; as we expect, this is an even smaller depth threshold than the  $D \geq 0.18/p_2$  predicted in [23]. For a current state-of-the-art two-qubit gates error of  $p_2 = 10^{-3}$  (see [36] and data tables in [29]), our approach predicts that circuits with depth  $D \geq 110$  are already in the regime of certified classical superiority.

In a more general setting, our approach also allows to predict an effective circuit volume, i.e., total number of gates obtained from Eq. (13), beyond which quantum advantage for the specific problem under study is no longer possible. The effective circuit volume is visualised in Fig. 8 (dark blue line) for the G12 MAX-CUT instance above for a QPU with two-qubit gate error given by  $p_2 = 0.01$ .

For large system sizes, we see that our depth threshold saturates at a constant value  $\frac{1}{2p_2} c \ln(2)$  for fixed  $c$  (dotted blue line) which is below the depth threshold derived in [23] based on relative entropy contraction results (cyan line). This shows that quantum advantage is lost at a shorter depth than originally predicted for large problem sizes. In fact, it can be proven analytically that our depth threshold is tighter than [23] for any  $c$  and  $p_2$  values (see appendix D). One can also prove that in the event of the threshold depth still keeping some dependency in the number of qubits  $n$ , our condition Eq. (14) would still be tighter than the depth

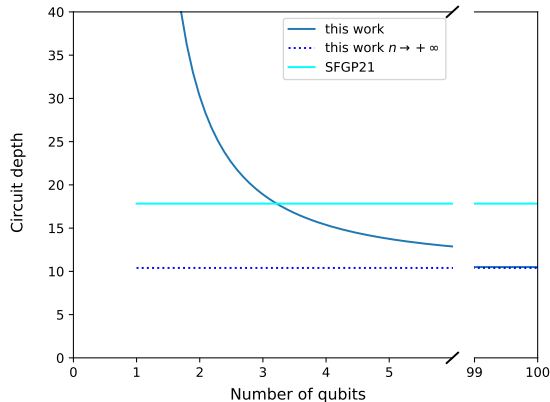


Figure 8: **Circuit size threshold above which quantum advantage is out of reach** (for arbitrary  $c$  and  $p_2$  values; here  $c = 0.3$  and  $p_2 = 0.01$ ). ‘This work’ corresponds to the newly derived circuit-size bound obtained from Eq. (13) (dark blue solid line) while SFGP21 (light blue solid line) is the depth condition previously derived in [23]. We cut the x-axis to show the threshold behavior in the  $n \rightarrow \infty$  limit.

threshold from [23] for large systems (see appendix D).

## V. CONCLUSION

Monitoring the accumulation of entropy density not only provides a complementary approach to circuit benchmarking, but more importantly, we have shown that combined with the theoretical framework of [23] it builds a much needed bridge between circuit-level and application-level benchmarking techniques.

To estimate the entropy on actual QPUs, we have explored two techniques, namely the classical shadows protocol and a SWAP test approach. In particular, we have highlighted the fact that the first protocol performs better for purity estimation of mixed states, while the SWAP test method should be preferred for close to pure states. Based on a combination of numerical simulation and experimental results on a superconducting QPU, we have observed

that entropy accumulation on dense programmable quantum circuits seems to be lower-bounded by a back-of-the-envelope model based on global depolarising noise. Therefore, knowledge of noise parameters deduced from calibration data can be exploited to estimate the entropy of the output of a hardware-efficient VQA circuit of any size via our model to later realise valuable predictions of their performance at application-level. Using this simple model for entropy accumulation, we have shown how to impose more stringent bounds on the circuit size above which quantum advantage is lost for hardware-efficient VQA circuits.

When estimating purities and its corresponding entropies, errors in the measurement seems to introduces systematic errors in the entropy estimate. It is important, specially when combined with the quantum advantage benchmarking from [23] to not overestimate the entropy of the system. Therefore, further work is needed to mitigate the effect of errors in the estimation of entropies but also ideally, to build theoretical techniques to provide guarantees, even certify, the validity of the entropy estimation.

Although depolarising noise seems to be an excellent model to predict entropy accumulation in superconducting circuits, our result hints that a more complete model for entropy accumulation is required, for example incorporating entropy decreasing error such as amplitude damping or coherent errors. This will be particularly critical for platforms where entropy-decreasing errors are dominant, like in photonic devices where photon loss is a dominant source of errors. For these platforms, generalisations of the application-level benchmarking approach to error parameters beyond entropy would probably be required in order to provide more accurate and stringent benchmarks of the performance of those platforms.

## ACKNOWLEDGMENTS

The experimental results were obtained using Rigetti’s Aspen-M-3 system. The authors thank Pauline Besserve for useful feedback on this manuscript, and Sean Thrasher and Chirag Wadhwa for valuable discussions. R.G.-P. and K. H. were supported by the EPSRC-funded project Benchmarking Quantum Advantage.

[1] D. Gottesman, Class of quantum error-correcting codes saturating the quantum hamming bound,

Physical Review A **54**, 1862 (1996).

- [2] D. Gottesman, An Introduction to Quantum Error Correction and Fault-Tolerant Quantum Computation (2009), arXiv:0904.2557 [quant-ph].
- [3] J. Roffe, Quantum error correction: an introductory guide, Contemporary Physics **60**, 226 (2019).
- [4] J. Preskill, Quantum Computing in the NISQ era and beyond, Quantum **2**, 79 (2018), publisher: Verein zur Förderung des Open Access Publizierens in den Quantenwissenschaften.
- [5] K. Bharti, A. Cervera-Lierta, T. H. Kyaw, T. Haug, S. Alperin-Lea, A. Anand, M. Degroote, H. Heimonen, J. S. Kottmann, T. Menke, *et al.*, Noisy intermediate-scale quantum algorithms, Reviews of Modern Physics **94**, 015004 (2022).
- [6] F. Arute, K. Arya, R. Babbush, D. Bacon, J. C. Bardin, R. Barends, R. Biswas, S. Boixo, F. G. S. L. Brandao, D. A. Buell, B. Burkett, Y. Chen, Z. Chen, B. Chiaro, R. Collins, W. Courtney, A. Dunsworth, E. Farhi, B. Foxen, A. Fowler, C. Gidney, M. Giustina, R. Graff, K. Guerin, S. Habegger, M. P. Harrigan, M. J. Hartmann, A. Ho, M. Hoffmann, T. Huang, T. S. Humble, S. V. Isakov, E. Jeffrey, Z. Jiang, D. Kafri, K. Kechedzhi, J. Kelly, P. V. Klimov, S. Knysh, A. Korotkov, F. Kostritsa, D. Landhuis, M. Lindmark, E. Lucero, D. Lyakh, S. Mandrà, J. R. McClean, M. McEwen, A. Megrant, X. Mi, K. Michielsen, M. Mohseni, J. Mutus, O. Naaman, M. Neeley, C. Neill, M. Y. Niu, E. Ostby, A. Petukhov, J. C. Platt, C. Quintana, E. G. Rieffel, P. Roushan, N. C. Rubin, D. Sank, K. J. Satzinger, V. Smelyanskiy, K. J. Sung, M. D. Trevithick, A. Vainsencher, B. Villalonga, T. White, Z. J. Yao, P. Yeh, A. Zalcman, H. Neven, and J. M. Martinis, Quantum supremacy using a programmable superconducting processor, Nature **574**, 505 (2019), number: 7779 Publisher: Nature Publishing Group.
- [7] H.-S. Zhong, H. Wang, Y.-H. Deng, M.-C. Chen, L.-C. Peng, Y.-H. Luo, J. Qin, D. Wu, X. Ding, Y. Hu, P. Hu, X.-Y. Yang, W.-J. Zhang, H. Li, Y. Li, X. Jiang, L. Gan, G. Yang, L. You, Z. Wang, L. Li, N.-L. Liu, C.-Y. Lu, and J.-W. Pan, Quantum computational advantage using photons, Science **370**, 1460 (2020), publisher: American Association for the Advancement of Science.
- [8] H.-S. Zhong, Y.-H. Deng, J. Qin, H. Wang, M.-C. Chen, L.-C. Peng, Y.-H. Luo, D. Wu, S.-Q. Gong, H. Su, Y. Hu, P. Hu, X.-Y. Yang, W.-J. Zhang, H. Li, Y. Li, X. Jiang, L. Gan, G. Yang, L. You, Z. Wang, L. Li, N.-L. Liu, J. J. Renema, C.-Y. Lu, and J.-W. Pan, Phase-Programmable Gaussian Boson Sampling Using Stimulated Squeezed Light, Physical Review Letters **127**, 180502 (2021), publisher: American Physical Society.
- [9] S. Yu, Z.-P. Zhong, Y. Fang, R. B. Patel, Q.-P. Li, W. Liu, Z. Li, L. Xu, S. Sagona-Stophel, E. Mer, S. E. Thomas, Y. Meng, Z.-P. Li, Y.-Z. Yang, Z.-A. Wang, N.-J. Guo, W.-H. Zhang, G. K. Tranmer, Y. Dong, Y.-T. Wang, J.-S. Tang, C.-F. Li, I. A. Walmsley, and G.-C. Guo, A universal programmable Gaussian boson sampler for drug discovery, Nature Computational Science **3**, 839 (2023), number: 10 Publisher: Nature Publishing Group.
- [10] J. M. Arrazola and T. R. Bromley, Using Gaussian Boson Sampling to Find Dense Subgraphs, Physical Review Letters **121**, 030503 (2018), publisher: American Physical Society.
- [11] S. Aaronson and S.-H. Hung, Certified Randomness from Quantum Supremacy (2023), arXiv:2303.01625 [quant-ph].
- [12] M. Cerezo, A. Arrasmith, R. Babbush, S. C. Benjamin, S. Endo, K. Fujii, J. R. McClean, K. Mitarai, X. Yuan, L. Cincio, and P. J. Coles, Variational quantum algorithms, Nature Reviews Physics **3**, 625 (2021), number: 9 Publisher: Nature Publishing Group.
- [13] E. Farhi, J. Goldstone, and S. Gutmann, A Quantum Approximate Optimization Algorithm (2014), arXiv:1411.4028 [quant-ph].
- [14] A. Peruzzo, J. McClean, P. Shadbolt, M.-H. Yung, X.-Q. Zhou, P. J. Love, A. Aspuru-Guzik, and J. L. O'Brien, A variational eigenvalue solver on a photonic quantum processor, Nature Communications **5**, 4213 (2014), number: 1 Publisher: Nature Publishing Group.
- [15] Y. Kim, A. Eddins, S. Anand, K. X. Wei, E. van den Berg, S. Rosenblatt, H. Nayfeh, Y. Wu, M. Zaletel, K. Temme, and A. Kandala, Evidence for the utility of quantum computing before fault tolerance, Nature **618**, 500 (2023), number: 7965 Publisher: Nature Publishing Group.
- [16] J. Tindall, M. Fishman, E. M. Stoudenmire, and D. Sels, Efficient Tensor Network Simulation of IBM's Eagle Kicked Ising Experiment, PRX Quantum **5**, 010308 (2024), publisher: American Physical Society.
- [17] T. Begušić, J. Gray, and G. K.-L. Chan, Fast and converged classical simulations of evidence for the utility of quantum computing before fault tolerance, Science Advances **10**, eadk4321 (2024), publisher: American Association for the Advancement of Science.
- [18] E. Magesan, J. M. Gambetta, and J. Emerson, Characterizing quantum gates via randomized benchmarking, Physical Review A **85**, 042311 (2012), publisher: American Physical Society.
- [19] E. Nielsen, J. K. Gamble, K. Rudinger, T. Scholten, K. Young, and R. Blume-Kohout, Gate Set Tomography, Quantum **5**, 557 (2021), publisher: Verein zur Förderung des Open Access Publizierens in den Quantenwissenschaften.
- [20] A. W. Cross, L. S. Bishop, S. Sheldon, P. D. Nation, and J. M. Gambetta, Validating quantum computers using randomized model circuits, Physical Review A **100**, 032328 (2019), publisher: American Physical Society.
- [21] S. Martiel, T. Ayril, and C. Allouche, Benchmarking Quantum Coprocessors in an Application-

- Centric, Hardware-Agnostic, and Scalable Way, IEEE Transactions on Quantum Engineering **2**, 1 (2021).
- [22] P.-L. Dallaire-Demers, M. Stechly, J. F. Gonthier, N. T. Bashige, J. Romero, and Y. Cao, An application benchmark for fermionic quantum simulations (2020), arXiv:2003.01862 [quant-ph].
- [23] D. Stilck França and R. García-Patrón, Limitations of optimization algorithms on noisy quantum devices, Nature Physics **17**, 1221 (2021), number: 11 Publisher: Nature Publishing Group.
- [24] O. Shtanko, Y. A. Kharkov, L. P. García-Pintos, and A. V. Gorshkov, Classical Models of Entanglement in Monitored Random Circuits (2020), arXiv:2004.06736 [cond-mat, physics:quant-ph].
- [25] M. Zhang, C. Wang, S. Dong, H. Zhang, Y. Han, and L. He, Entanglement entropy scaling of noisy random quantum circuits in two dimensions, Physical Review A **106**, 052430 (2022), publisher: American Physical Society.
- [26] A. Elben, S. T. Flammia, H.-Y. Huang, R. Kueng, J. Preskill, B. Vermersch, and P. Zoller, The randomized measurement toolbox, Nature Reviews Physics **5**, 9 (2023), number: 1 Publisher: Nature Publishing Group.
- [27] A. Elben, R. Kueng, H.-Y. R. Huang, R. van Bijnen, C. Kokail, M. Dalmonte, P. Calabrese, B. Kraus, J. Preskill, P. Zoller, and B. Vermersch, Mixed-State Entanglement from Local Randomized Measurements, Physical Review Letters **125**, 200501 (2020), publisher: American Physical Society.
- [28] Qiskit.
- [29] Google willow quantum chip.
- [30] H.-Y. Huang, R. Kueng, and J. Preskill, Predicting many properties of a quantum system from very few measurements, Nature Physics **16**, 1050 (2020), number: 10 Publisher: Nature Publishing Group.
- [31] H. Buhrman, R. Cleve, J. Watrous, and R. de Wolf, Quantum Fingerprinting, Physical Review Letters **87**, 167902 (2001), publisher: American Physical Society.
- [32] J. C. Garcia-Escartin and P. Chamorro-Posada, swap test and Hong-Ou-Mandel effect are equivalent, Physical Review A **87**, 052330 (2013), publisher: American Physical Society.
- [33] D. F. Perez-Ramirez, Variational quantum algorithms for combinatorial optimization, arXiv preprint arXiv:2407.06421 (2024).
- [34] P. J. O'Malley, R. Babbush, I. D. Kivlichan, J. Romero, J. R. McClean, R. Barends, J. Kelly, P. Roushan, A. Tranter, N. Ding, *et al.*, Scalable quantum simulation of molecular energies, Physical Review X **6**, 031007 (2016).
- [35] S. Stanisic, J. L. Bosse, F. M. Gambetta, R. A. Santos, W. Mruczkiewicz, T. E. O'Brien, E. Ostby, and A. Montanaro, Observing ground-state properties of the fermi-hubbard model using a scalable algorithm on a quantum computer, Nature communications **13**, 5743 (2022).
- [36] R. Acharya, L. Aghababaie-Beni, I. Aleiner, T. I. Andersen, M. Ansmann, F. Arute, K. Arya, A. Asfaw, N. Astrakhantsev, J. Atalaya, *et al.*, Quantum error correction below the surface code threshold, arXiv preprint arXiv:2408.13687 (2024).
- [37] W. Hoeffding, Probability inequalities for sums of bounded random variables, The collected works of Wassily Hoeffding , 409 (1994).
- [38] J. P. Gaebler, A. M. Meier, T. R. Tan, R. Bowler, Y. Lin, D. Hanneke, J. D. Jost, J. Home, E. Knill, D. Leibfried, *et al.*, Randomized benchmarking of multiqubit gates (2012).

## Appendix A: Analytical model for the Renyi entropy density evolution in a VQA circuit with classical shadows and readout noise

In this section, we adapt the heuristic model from Eq. (6) to take into account the effect of noise in the measurement circuit of the classical shadows protocol and readout errors on the Renyi-2 entropy and purity evolution.

We assume that we can represent local depolarising noise, and readout and measurement circuit noise by two successive global depolarising noise channels  $\mathcal{N}_P : \rho \mapsto (1-P)\rho + P\frac{I}{2^n}$  and  $\mathcal{N}_{P_M} : \rho \mapsto (1-P_M)\rho + P_M\frac{I}{2^n}$  (for an  $n$ -qubit quantum state  $\rho$ ) with depolarising probabilities  $P$  and  $P_M$  respectively, placed at the very end of the ideal circuit. As we did in Eq. 5, we can link those two probabilities to fitting parameters  $\alpha_1, \alpha_2$  (depolarising), and  $\beta$  (readout) by equating the probabilities of no error occurring in both our local noise model and global noise model:

$$1 - P := (1 - p_1)^{|1Q \text{ gates}|} (1 - p_2)^{|2Q \text{ gates}|}, \quad (\text{A1})$$

$$= (1 - p_1)^{2nD} (1 - p_2)^{(n-1)D}, \quad (\text{A2})$$

$$:= e^{-2\alpha_1 nD} e^{-\alpha_2 (n-1)D}, \quad (\text{A3})$$

and

$$1 - P_M := (1 - p_m)^n := e^{-\beta n}, \quad (\text{A4})$$

where  $\alpha_i = \ln((1 - p_i)^{-1})$  and  $\beta = \ln((1 - p_m)^{-1})$  are the local depolarising error probabilities  $p_i$  and  $p_m$  in the low noise limit:  $\alpha_i \approx p_i$  and  $\beta \approx p_m$ . Our new model for the purity is given by

$$\text{Tr}[\rho_D^2] = (1 - 2^{-n})(e^{-2(2\alpha_1 nD + \alpha_2 (n-1)D + \beta n)} - 1) + 1. \quad (\text{A5})$$

## Appendix B: Purity estimate from the classical shadows protocol with Pauli basis measurements

In this section dedicated to purity estimation using the Pauli-basis classical shadows protocol from [30], we provide a simple expression for the corresponding purity estimate in subsection B 1, give an upper bound on the sampling cost in B 2, and discuss the existence of a systematic error in the purity estimate of a derandomised version of the classical shadows technique in B 3.

### 1. Purity estimate

Consider the purity estimate from the classical shadows protocol given in the paper [26]:

$$\hat{P}_{\text{Shadows}}^{(M,K)} := \frac{1}{M(M-1)} \sum_{m \neq m'} \text{Tr}[\hat{\rho}^{(m)} \hat{\rho}^{(m')}], \quad (\text{B1})$$

where

$$\hat{\rho}^{(m)} := \frac{1}{K} \sum_{k=1}^K \bigotimes_{n=1}^N \left( 3 \left( U_n^{(m)} \right)^\dagger |s_n^{(m,k)}\rangle \langle s_n^{(m,k)}| U_n^{(m)} - I \right). \quad (\text{B2})$$

For the special case of Pauli measurements, it is possible to further simplify the formula for the purity estimate. First, consider the product  $\hat{\rho}^{(m)} \hat{\rho}^{(m')}$ :

$$\hat{\rho}^{(m)}\hat{\rho}^{(m')} = \frac{1}{K^2} \sum_{k,k'=1}^K \bigotimes_{n=1}^N \left( 3 \left( U_n^{(m)} \right)^\dagger \left| s_n^{(m,k)} \right\rangle \left\langle s_n^{(m,k)} \right| U_n^{(m)} - I \right) \left( 3 \left( U_n^{(m')} \right)^\dagger \left| s_n^{(m',k')} \right\rangle \left\langle s_n^{(m',k')} \right| U_n^{(m')} - I \right), \quad (\text{B3})$$

$$= \frac{1}{K^2} \sum_{k,k'=1}^K \bigotimes_{n=1}^N \quad (\text{B4})$$

$$\left( 9 \left( U_n^{(m)} \right)^\dagger \left| s_n^{(m,k)} \right\rangle \left\langle s_n^{(m,k)} \right| U_n^{(m)} \left( U_n^{(m')} \right)^\dagger \left| s_n^{(m',k')} \right\rangle \left\langle s_n^{(m',k')} \right| U_n^{(m')} \right. \quad (\text{B5})$$

$$\left. - 3 \left( U_n^{(m)} \right)^\dagger \left| s_n^{(m,k)} \right\rangle \left\langle s_n^{(m,k)} \right| U_n^{(m)} - 3 \left( U_n^{(m')} \right)^\dagger \left| s_n^{(m',k')} \right\rangle \left\langle s_n^{(m',k')} \right| U_n^{(m')} + I \right). \quad (\text{B6})$$

Taking the trace of the above product of shadows and exploiting the linearity of the trace and the fact that the trace of a tensor product is the product of the traces, we have

$$\text{Tr} \left[ \hat{\rho}^{(m)} \hat{\rho}^{(m')} \right] = \frac{1}{K^2} \sum_{k,k'=1}^K \prod_{n=1}^N \quad (\text{B7})$$

$$\left( 9 \text{Tr} \left[ \left( U_n^{(m)} \right)^\dagger \left| s_n^{(m,k)} \right\rangle \left\langle s_n^{(m,k)} \right| U_n^{(m)} \left( U_n^{(m')} \right)^\dagger \left| s_n^{(m',k')} \right\rangle \left\langle s_n^{(m',k')} \right| U_n^{(m')} \right] \right. \quad (\text{B8})$$

$$\left. - 3 \text{Tr} \left[ \left( U_n^{(m)} \right)^\dagger \left| s_n^{(m,k)} \right\rangle \left\langle s_n^{(m,k)} \right| U_n^{(m)} \right] \right. \quad (\text{B9})$$

$$\left. - 3 \text{Tr} \left[ \left( U_n^{(m')} \right)^\dagger \left| s_n^{(m',k')} \right\rangle \left\langle s_n^{(m',k')} \right| U_n^{(m')} \right] + \text{Tr}[I] \right), \quad (\text{B10})$$

where each of the traces above are traces of 2-by-2 matrices, so that

$$\text{Tr}[I] = 2. \quad (\text{B11})$$

As the trace is cyclic and the  $U_n^{(m)}$  are unitary matrices and since the  $|s_n^{(m',k')}\rangle$  form an orthonormal family of quantum states, we deduce that

$$\text{Tr} \left[ \left( U_n^{(m)} \right)^\dagger \left| s_n^{(m,k)} \right\rangle \left\langle s_n^{(m,k)} \right| U_n^{(m)} \right] = 1, \quad (\text{B12})$$

$$\text{Tr} \left[ \left( U_n^{(m')} \right)^\dagger \left| s_n^{(m',k')} \right\rangle \left\langle s_n^{(m',k')} \right| U_n^{(m')} \right] = 1. \quad (\text{B13})$$

Simplifying (B8) needs further work, however for the special case of Pauli measurements, possible values for this trace can be restricted to the three values  $\{0, 1, 1/2\}$ . To see this, first notice that since the trace is cyclic,

$$\text{Tr} \left[ \left( U_n^{(m)} \right)^\dagger \left| s_n^{(m,k)} \right\rangle \left\langle s_n^{(m,k)} \right| U_n^{(m)} \left( U_n^{(m')} \right)^\dagger \left| s_n^{(m',k')} \right\rangle \left\langle s_n^{(m',k')} \right| U_n^{(m')} \right] \quad (\text{B14})$$

$$= \text{Tr} \left[ \left\langle s_n^{(m,k)} \right| U_n^{(m)} \left( U_n^{(m')} \right)^\dagger \left| s_n^{(m',k')} \right\rangle \left\langle s_n^{(m',k')} \right| U_n^{(m')} \left( U_n^{(m)} \right)^\dagger \left| s_n^{(m,k)} \right\rangle \right], \quad (\text{B15})$$

$$= \text{Tr} \left[ \left| \left\langle s_n^{(m,k)} \right| U_n^{(m)} \left( U_n^{(m')} \right)^\dagger \left| s_n^{(m',k')} \right\rangle \right|^2 \right], \quad (\text{B16})$$

$$= \left| \left\langle s_n^{(m,k)} \right| U_n^{(m)} \left( U_n^{(m')} \right)^\dagger \left| s_n^{(m',k')} \right\rangle \right|^2 = \gamma_{n,m,m',k,k'}, \quad (\text{B17})$$



where  $s_n^{(m,k)}, s_n^{(m',k')} \in \{0, 1\}$  and  $U_n^{(m)}, U_n^{(m')} \in \{H, HS^\dagger, I\}$ . Exploring all possible combinations for  $s_n^{(m,k)}, s_n^{(m',k')}, U_n^{(m)}, U_n^{(m')}$ , it can then be shown that  $\gamma_{n,m,m',k,k'}$  can only take three different kinds of values: this is summarised in table I.

$U_n^{(m)} \times (U_n^{(m')})^\dagger$	$ \langle 0  \cdot  0\rangle ^2$	$ \langle 0  \cdot  1\rangle ^2$	$ \langle 1  \cdot  0\rangle ^2$	$ \langle 1  \cdot  1\rangle ^2$
$H \times H = I$	1	0	0	1
$H \times SH = HSH$	1/2	1/2	1/2	1/2
$H \times I = H$	1/2	1/2	1/2	1/2
$HS^\dagger \times H = HS^\dagger H$	1/2	1/2	1/2	1/2
$HS^\dagger \times SH = I$	1	0	0	1
$HS^\dagger \times I = HS^\dagger$	1/2	1/2	1/2	1/2
$I \times H = H$	1/2	1/2	1/2	1/2
$I \times SH = SH$	1/2	1/2	1/2	1/2
$I \times I = I$	1	0	0	1

Table I: Possible values for  $\gamma_{n,m,m',k,k'}$  depending on the value of  $s_n^{(m,k)}, s_n^{(m',k')}, U_n^{(m)}, U_n^{(m')}$

$$\text{where } \gamma_{n,m,m',k,k'} := \left| \langle s_n^{(m,k)} | U_n^{(m)} (U_n^{(m')})^\dagger | s_n^{(m',k')} \rangle \right|^2$$

Finally, combining all previous results for the trace we conclude that, for Pauli measurements, the purity estimate can be simplified as

$$\hat{P}_{\text{Shadows}}^{(M,K)} = \frac{1}{M(M-1)} \sum_{m \neq m'} \frac{1}{K^2} \sum_{k,k'=1}^K \prod_{n=1}^N (9 \times \gamma_{n,m,m',k,k'} - 4). \quad (\text{B18})$$

Noting that  $\gamma_{n,m,m',k,k'} = \gamma_{n,m',m,k,k'}$ , this further simplifies to

$$\hat{P}_{\text{Shadows}} := \hat{P}_{\text{Shadows}}^{(M,K)} = \frac{2}{M(M-1)} \sum_m \sum_{m' | m' < m} \frac{1}{K^2} \sum_{k,k'=1}^K \prod_{n=1}^N (9 \times \gamma_{n,m,m',k,k'} - 4), \quad (\text{B19})$$

where

$$\gamma := \gamma_{n,m,m',k,k'} = \left| \langle s_n^{(m,k)} | U_n^{(m)} (U_n^{(m')})^\dagger | s_n^{(m',k')} \rangle \right|^2, \quad (\text{B20})$$

is given by table I.

## 2. Upper bound on the sampling cost

Fix accuracy parameters  $\delta, \epsilon > 0$  and  $K = 1$ . From theorem S4 and proposition S4 of the supplementary material of [30], we know that a collection of  $M$  independent classical shadows such that

$$M \leq 2 \ln(2/\delta) \frac{34}{\epsilon^2} 8 \times 4^n \|S\|_\infty^2, \quad (\text{B21})$$

i.e.,

$$M \leq \ln(2/\delta) \frac{544}{\epsilon^2} 4^n, \quad (\text{B22})$$

using the fact that  $\|S\|_\infty^2 = 1$  where  $S$  is the SWAP operator, allow for accurately predicting the purity  $\text{Tr}[\rho^2]$  of state  $\rho$ :

$$|\hat{P}_{\text{Shadows}} - \text{Tr}[\rho^2]| \leq \epsilon, \quad (\text{B23})$$

with probability at least  $1 - \delta$ .

### 3. Systematic error in the derandomized version of the classical shadows protocol

Changing circuits is relatively costly in execution time for some platforms like superconducting qubits. Since our entropy accumulation experiments were limited in number of qubits ( $n = 3$ ) and therefore we were expecting to see the occurrence of most measurements and in similar number, we initially opted for a derandomization of the measurement choice where we consider one by one all of the  $3^3 = 27$  possible measurement settings with  $K = 1,000$  classical snapshots of the output state for each of them. The equivalent of Fig. 4 for experimental entropy accumulation but in the case of derandomized measurements of the classical shadows protocol corresponds to Fig. 9, where we can observe the presence of a systematic bias in the purity or Renyi-2 entropy density estimate provided by the classical shadows protocol.

## Appendix C: Purity estimate from the SWAP test protocol

This section focuses on purity estimation via the SWAP test protocol [31]. In subsection C 1, we give an expression for the corresponding purity estimate, and an upper bound on the sampling cost of the protocol is provided in subsection C 2.

### 1. Purity estimate from the original SWAP Test protocol

The purity  $\text{Tr}[\rho^2]$  of a quantum state  $\rho$  can be rewritten as an expectation value of the SWAP observable  $S$  with respect to quantum state  $\rho^{\otimes 2}$ , i.e.,  $\text{Tr}[\rho^2] = \text{Tr}[S\rho \otimes \rho] = \langle S \rangle_{\rho \otimes \rho}$  where for any pure states  $|\Psi\rangle, |\Phi\rangle$ ,  $S|\Psi\rangle|\Phi\rangle = |\Phi\rangle|\Psi\rangle$ . Since the SWAP observable  $S$  has two eigenvalues  $\pm 1$ , we can decompose it into a linear combination of their corresponding projectors:  $S = \Pi_{+1} - \Pi_{-1}$  where  $\Pi_{+1}$  and  $\Pi_{-1}$  are the projectors on the  $+1$  and  $-1$  eigenspaces respectively. This means that the purity can be written as  $\text{Tr}[\rho^2] = \text{Tr}[\Pi_{+1}\rho \otimes \rho] - \text{Tr}[\Pi_{-1}\rho \otimes \rho]$ .

Consider the SWAP test circuit from Fig. 5a which is the original SWAP test protocol from [31] to distinguish between two quantum states. Right before measurement, the quantum register is in state

$$\rho' := |0\rangle\langle 0| \otimes \Pi_{+1}(\rho \otimes \rho)\Pi_{+1} + |1\rangle\langle 1| \otimes \Pi_{-1}(\rho \otimes \rho)\Pi_{-1}. \quad (\text{C1})$$

Therefore, measuring the first qubit, we get outcome  $i \in \{0, 1\}$  with probability

$$P(i) = \text{Tr}[|i\rangle\langle i| \otimes I \rho'], \quad (\text{C2})$$

$$= \text{Tr}[|i\rangle\langle i| \otimes I(|0\rangle\langle 0| \otimes \Pi_{+1}(\rho \otimes \rho)\Pi_{+1} + |1\rangle\langle 1| \otimes \Pi_{-1}(\rho \otimes \rho)\Pi_{-1})], \quad (\text{C3})$$

$$= \text{Tr}[|i\rangle\langle i| \otimes \Pi_{(-1)^i}(\rho \otimes \rho)\Pi_{(-1)^i}], \quad (\text{C4})$$

$$= \text{Tr}[\Pi_{(-1)^i}\rho \otimes \rho]. \quad (\text{C5})$$

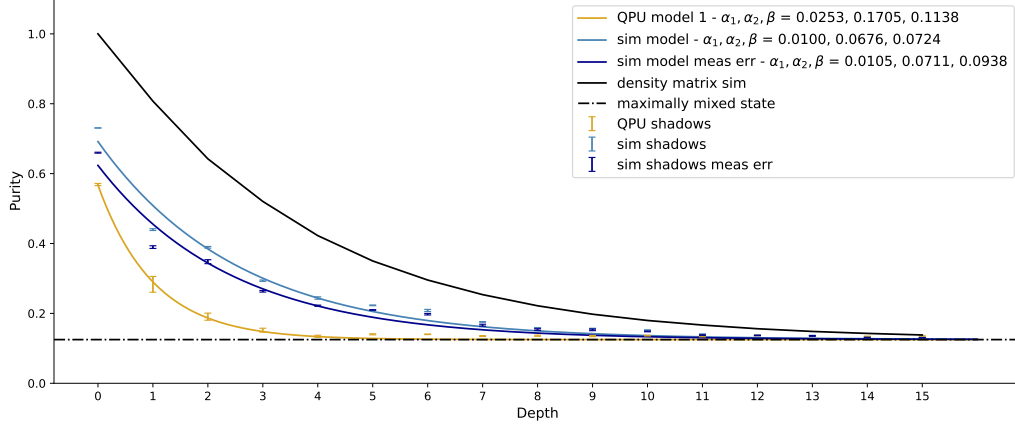
Thus it is possible to get the purity of  $\rho$  from this circuit via

$$\text{Tr}[\rho^2] = \text{Tr}[\Pi_{+1}\rho \otimes \rho] - \text{Tr}[\Pi_{-1}\rho \otimes \rho], \quad (\text{C6})$$

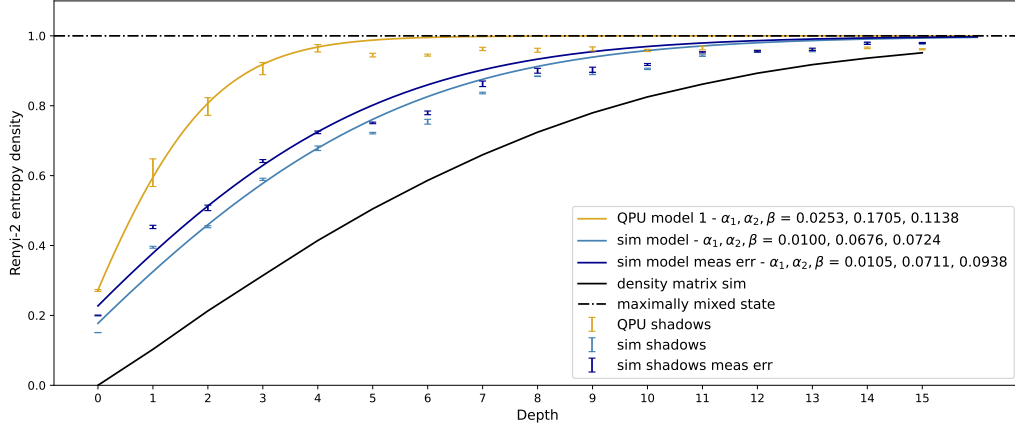
$$= P(0) - P(1). \quad (\text{C7})$$

In practice with  $M$  measurements, we can obtain the following purity estimate:

$$\hat{P}_{\text{SWAP}} = \frac{M_0 - M_1}{M}, \quad (\text{C8})$$



(a) Purity



(b) Renyi entropy density

Figure 9: **Experimental results and validation of our heuristic model.** We consider a VQA circuit as in Fig. 1 applied to  $n = 3$  qubits, with fixed circuit parameters (fixed random seed `np.random.seed(837)`). Golden error bars give the purity and Renyi-2 entropy evolution as functions of circuit depth on Rigetti’s QPU Aspen-M-3 using the derandomized version of the protocol (with  $M = 3^3 = 27$  measurement settings considered in order). Each error bar was obtained by running the classical shadows protocol 3 times, and computing the average estimate and the standard deviation over those 3 samples. Results obtained in the same setting but using a local depolarising noise model ( $p_1 = 0.008$  and  $p_2 = 0.054$  from calibration data of Aspen-M-3) correspond to the blue error bars; dark (resp. light) blue error bars were obtained with (resp. without) readout errors from calibration data. The black solid lines show the purity and Renyi-2 entropy density evolution obtained via density matrix simulation under our local depolarising noise model. The black horizontal dash-dotted lines correspond to the purity or entropy density of the maximally mixed state  $\sigma_0 := I/2^n$ . Fit of our global depolarising heuristic model, where we have imposed that  $\alpha_2/\alpha_1 = p_2/p_1$ , corresponds to the solid golden and blue lines.

$$\hat{P}_{\text{SWAP}} = 2 \frac{M_0}{M} - 1 = 1 - 2 \frac{M_1}{M}, \quad (\text{C9})$$

where  $M_i$  is the number of times outcome  $i$  was measured in the circuit from Fig. 5a.

## 2. Upper bound on the sampling cost

We want to derive an upper bound on the sampling cost  $M$  for purity estimation via the SWAP test protocol. We achieve this by using Hoeffding's inequality [37] which provides an upper bound on the probability  $\delta$  that a sum of bounded independent variables deviates from its expected value by more than some amount  $\epsilon$ .

Fix accuracy parameters  $\epsilon, \delta > 0$ . Let  $Z_1, \dots, Z_M$  be independent bounded random variables with  $Z_j \in [a, b]$  for all  $j$ , where  $-\infty < a \leq b < \infty$ . Then, Hoeffding's inequality states that

$$\delta := P \left( \left| \frac{1}{M} \sum_{j=1}^M (Z_j - \mathbf{E}[Z_j]) \right| \geq \epsilon \right) \leq 2e^{-\frac{2M\epsilon^2}{(b-a)^2}}, \quad (\text{C10})$$

for all  $\epsilon \geq 0$ .

In the case of purity estimation using the SWAP test, the target expected value is the exact purity  $P := \text{Tr}[\rho^2]$  and the sum of bounded independent variables is the SWAP test purity estimate from Eq. (C9)

$$\hat{P}_{\text{SWAP}} = 1 - 2 \frac{M_1}{M} \quad (\text{C11})$$

$$= 1 - 2 \frac{\sum_{j=1}^M i_j}{M}, \quad (\text{C12})$$

where  $i_j \in \{0, 1\}$  is the  $j^{\text{th}}$  measurement outcome of the SWAP test circuit from Fig. 5a,  $M$  is the total number of measurements, and  $M_1$  is the number of times that outcome 1 was obtained (out of those  $M$  measurements).

So, we have

$$Z_j := 1 - 2i_j, \quad (\text{C13})$$

As  $i_j \in \{0, 1\}$  for all  $j$ , those random variables satisfy

$$-\infty < -1 \leq Z_j \leq 1 < \infty \quad \text{and} \quad \mathbf{E}[Z_j] = \mathbf{E}[Z_1] = P \quad (\text{C14})$$

Therefore, Hoeffding's inequality gives

$$\delta := P \left( \left| \frac{1}{M} \sum_{j=1}^M (1 - 2i_j) - P \right| \geq \epsilon \right) \leq 2e^{-\frac{2M\epsilon^2}{(1+1)^2}}, \quad (\text{C15})$$

$$\delta = P \left( \left| \frac{1}{M} \left( M - 2 \sum_{j=1}^M i_j \right) - P \right| \geq \epsilon \right) \leq 2e^{-\frac{M\epsilon^2}{2}}, \quad (\text{C16})$$

$$\delta = P \left( \left| \frac{1}{M} (M - 2M_1) - P \right| \geq \epsilon \right) \leq 2e^{-\frac{M\epsilon^2}{2}}, \quad (\text{C17})$$

$$\delta = P \left( \left| \hat{P}_{\text{SWAP}} - P \right| \geq \epsilon \right) \leq 2e^{-\frac{M\epsilon^2}{2}}. \quad (\text{C18})$$

This means that

$$\ln(\delta/2) \leq -\frac{M\epsilon^2}{2}, \quad (\text{C19})$$

$$M \leq 2 \ln \left( \frac{2}{\delta} \right) \frac{1}{\epsilon^2}. \quad (\text{C20})$$

In other words, at most  $2 \times \ln\left(\frac{2}{\delta}\right) \times \frac{1}{\epsilon^2}$  measurements are necessary to obtain an  $\epsilon$ -accurate purity estimate with probability  $1 - \delta$ .

#### Appendix D: Circuit size boundary for reachable quantum advantage

In this section, we prove that our bound on the circuit size boundary for reachable quantum advantage Eq. D2 is tighter than this of [23] for a large number of qubits.

The circuit size condition for classical superiority from [23] is

$$D \geq \frac{1}{2\alpha} \ln(1-c)^{-1}, \quad (\text{D1})$$

while at  $n \rightarrow \infty$ , ours is

$$D \geq \frac{1}{2\alpha} c \ln(2). \quad (\text{D2})$$

Let  $f(c) := c \ln(2) - \ln((1-c)^{-1}) = c \ln(2) + \ln(1-c), \forall c \in [0, 1]$ . We have  $\frac{df}{dc}(c) = \ln(2) - \frac{1}{1-c}$ , which can be shown to satisfy  $\frac{df}{dc}(c) < 0, \forall c \in [0, 1]$ . Therefore  $f$  is a strictly decreasing function on its domain  $c \in [0, 1]$ . Since  $f(0) = 0$ , we conclude that  $f(c) \leq 0$  for all values of  $c \in [0, 1]$ . This means that for large problem sizes i.e.,  $n \rightarrow \infty$ , quantum advantage will be lost at a shorter depth Eq. (D2) than this predicted in [23]. Note that the above argument remains valid even for the more realistic case where the entropy density threshold  $c$  keeps a dependency with the system size  $n$ , i.e.,  $c = c(n)$ . This is because the value  $c(n)$  remains the same input for both bounds and  $f(c) \leq 0$  for all values of  $c \in [0, 1]$  remains true irrespectively of the variables that may define  $c$  ( $n$  in our case or others).

#### Appendix E: Rigetti's Aspen-M-3 and link between calibration data and noise parameters

We link noise parameters of the noise model used for numerical simulations with typical calibration data given for a quantum device.

All QPU experiments shown in this article were run on Rigetti's 8-qubit Aspen-M-3 device (see Fig. 10). For one-qubit circuits, qubit #100 was used, for two-qubit circuits, qubits #100, 101 were used, for three-qubit circuits, #100, 101, 102, and so on. Calibration data from the day of our experiments is provided in table II.

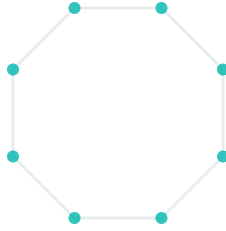


Figure 10: 8-qubit Aspen-M-3 QPU

Assuming local depolarising noise as the noise model on the device for classical simulations, it is possible to link one-qubit and two-qubit gate fidelities ( $F_1$  and  $F_2$ ) from calibration data to one-qubit and two-qubit depolarising probabilities ( $p_1$  and  $p_2$ ) as follows:

$$p_1 = 2(1 - F_1), \quad (\text{E1})$$

$$p_2 = \frac{4}{3}(1 - F_2), \quad (\text{E2})$$

where we have used the fact that the fidelity between a pure state  $|\Psi\rangle$  and a mixed state  $\rho$  is  $F = \langle\Psi|\rho|\Psi\rangle$  and taking for  $|\Psi\rangle$  a pure state evolved with some ideal gate  $U$ , and for  $\rho$  a pure state evolved with  $U$  followed by a depolarising channel (e.g., see [38]). For our classical simulations, we considered the median sim RB fidelity (one-qubit gate fidelity) and the median CZ fidelity (two-qubit gate fidelity) in agreement with the two-qubit gates of our VQA ansatz.

For classical simulations where readout errors were included, we estimated the probabilities  $P(0|1)$  and  $P(1|0)$  on Aspen-M-3, and obtained

$$P(0|1) = 0.03484722222 \quad P(1|0) = 0.022177777, \quad (\text{E3})$$

where  $P(m|n)$  is the probability of obtaining outcome  $m$  instead of  $n$  due to readout error. In our heuristic model from Eq. (A5), adapted to take into account readout errors,  $p_m$  is related to  $P(0|1)$  and  $P(1|0)$  in the case where those have similar values (symmetric readout error).

Pair	fXY	fXY std err	fCZ	fCZ std err	Avg T1 ( $\mu\text{s}$ )	Avg T2 ( $\mu\text{s}$ )	Avg fActiveReset	Avg fRO
100–101	0.9614	0.007829	0.9598	0.0058	19.3	33.22	0.9943	0.941
100–107	0.8553	0.007008	0.9769	0.005897	27.2	45.47	0.996	0.944
101–102	0.9626	0.009064			21.36	32.92	0.996	0.9165
102–103	0.8409	0.01479	0.9711	0.007058	26.6	29.48	0.9858	0.9135
103–104	0.8534	0.006161	0.909	0.003757	31.31	43.49	0.8827	0.9455
104–105	0.812	0.007665	0.8917	0.004528	29.04	35.61	0.8945	0.945
105–106	0.9756	0.003552			27.46	15.55	0.9885	0.9735
106–107	0.9828	0.002881	0.9948	0.002183	32.39	39.13	0.9888	0.98

Qubit	T1 ( $\mu\text{s}$ )	T2 ( $\mu\text{s}$ )	f1QRB	f1QRB std err	f1Q sim. RB	f1Q sim. RB std err	fActiveReset	fRO
100	11.82	20.1	0.997	0.000175	0.9957	0.000109	0.9955	0.908
101	26.78	46.34	0.9997	0.000382	0.9989	5.61E-05	0.993	0.974
102	15.95	19.5	0.9977	0.00014	0.9959	0.000148	0.999	0.859
103	37.25	39.46	0.9953	0.000827	0.9869	0.000571	0.9725	0.968
104	25.36	47.52	0.8209	0.04649	0.8665	0.0576	0.793	0.923
105	32.72	23.71	0.9984	6.81E-05	0.9949	0.000161	0.996	0.967
106	22.2	7.401	0.999	4.9E-05	0.9973	0.000185	0.981	0.98
107	42.58	70.85	0.9995	6.44E-05	0.9989	2.96E-05	0.9965	0.98

Table II: Aspen-M-3 calibration data on December 9th, 2023 at 9:59pm (UK time)